Digital Deconvolution Microscopy: Development, Evaluation and Utilization in 3D quantitative studies of E-cadherin expression in skin of *Bufo arenarun* tadpoles

J. F. Adur, J. E. Diaz-Zamboni, N. B. Vicente, M. F. Izaguirre and **V. H. Casco***

Laboratorio de Microscopia, Facultad de Ingeniería, Universidad Nacional de Entre Ríos.
Ruta 11 km 10, Oro Verde, Entre Ríos, Argentina.

Deconvolution of three-dimensional (3D) fluorescence microscopy images using computational restoration algorithms may be seen as a cheaper alternative to modern 3D microscopy techniques. We have recently developed a digital deconvolution microscope based upon a standard upright fluorescence microscopy setup, which allows us to perform precise optical-sectioning procedures by positioning the sample at different focal depths. The acquired images are then treated using computational methods which use information regarding the image-formation process (deconvolution using the Point Spread Function, PSF). Processed images are used to perform a more accurate 3D quantification and analyses. The main objective of the present work is to evaluate the technique's steps and to analyze the usefulness of this method with the aid of a biological model. For that reason, we selected a 3D cell-adhesion skin model, based upon a specimen commonly used by our research group. In the present work we show what must be considered in order to obtain an adequate and precise quantification.

Keywords Deconvolution, PSF, 3D quantification, 3D image analyses, E-cadherin expression.

1. Introduction

Biology seeks to understand complex cellular functions and cell-environment interactions. In the quest to fulfill this goal, few results are as relevant to the researcher as three-dimensional (3D) images. Methods currently used to obtain 3D images include 3D fluorescence microscopy [1-2], which possesses the unique capability of examining bio-structures and physiological states in living cells, enabling the study of complex relationships between the function and structure of biological systems. Additionally, fluorescence permits the functional evaluation of the spatial and temporal distribution of specific cellular components.

Fluorescence techniques commonly used to obtain 3D images include confocal laser (CLM) [3-4] and digital deconvolution microscopy (DDM) [5-6]. Both perform optical-sectioning and minimize the contamination of out-of-focus contributions (from non-focal planes) in different manners. Confocal laser microscopy employs a physical filter (pinhole) placed before the detector, which rejects fluorescence from non-focal planes. On the other hand, digital deconvolution microscopy produces images which contain information from the focus plane, as well as out-of-focus contributions from non-focal planes, which may be eliminated or restored to their correct spatial position by mathematical methods (deconvolution) that require the optical system's transfer function. Both microscopy techniques have pros and cons that must be evaluated; nevertheless, both produce similar and excellent results as far as resolution is concerned [7-9]. In order to choose which one to use, several elements must be taken into account, such as sample characteristics, type of data and application required.

Both types of microscopy require specialized personnel and expensive equipment. Members of our research group have updated the fluorescence microscopy equipment available in our laboratory, succeeding in the implementation of a digital deconvolution microscopy setup. In the present work, we describe every step involved in the mentioned technique, the implementation strategies carried out and

* Corresponding author: e-mail: vcasco@bioingenieria.edu.ar, Phone: +54 343 4975100 int (120)

their evaluation. Lastly, results obtained when applying this technique to a biological model commonly used by our research group are described, analyzing both qualitative and quantitative aspects.

2. Technique's steps and implementation

Figure 1 is a diagram of the different steps followed in DDM. Briefly, the following steps are involved: optical-sectioning of the specimen under study (producing a 3D image stack), determination of the Point Spread Function (PSF), deconvolution of the 3D image stack, 3D visualization, 3D quantification and analyses.

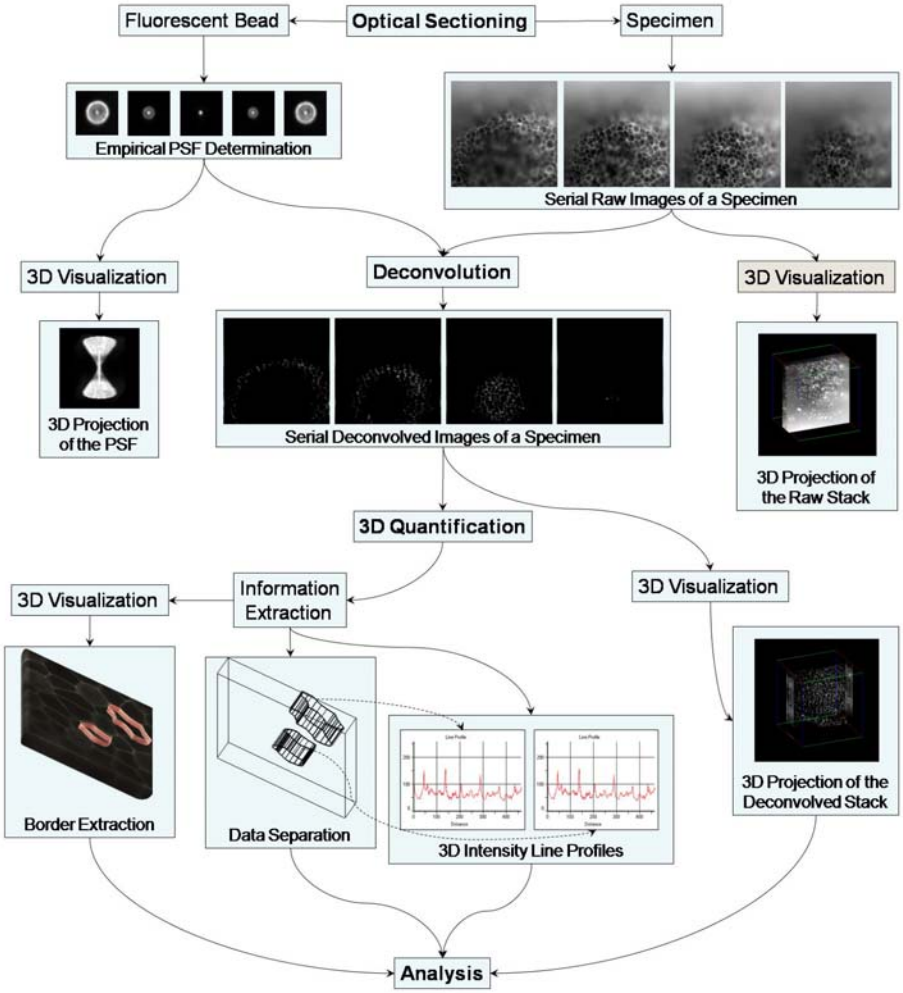

Fig. 1 Diagram of the steps involved in DDM.

2.1 Microscopy system

The system presented in the present work was built upon an Olympus BX50 upright epi-fluorescence microscope, equipped with a mercury lamp with emission peaks at 365/366, 404,7, 435, 546,1 and 577/579,1 nm, and a set of filters used to select the appropriate emission peaks. Objective corrected plan-apochromatic lens produce intermediate aberration-free images. The recording system consisted of a cooled monochromatic Apogee CCD camera of 14 bits of resolution, 768x512 pixel^2 sensor size, 9x9

μm^2 pixel size, mounted to the microscope by a mount C lens (0.5X). This device has high-resolution and sensitivity, wide dynamic range, and good geometrical stability, qualities particularly suitable for high-quality 2D (two-dimensional) and 3D studies [10].

2.2 Optical-sectioning

An electro-mechanic system (stepping motor + reduction box) attached to the BX50 microscope, enables the displacement of the stage at discrete intervals along the focal axis of the microscope (also known as Z axis or optical axis). This, in turn, enables optical-sectioning since 2D images are taken at different focal planes within the whole specimen. The stepping motor was used for it has a digital control, does not need feedback, has an easy speed control, low cost, simple interface and minimum maintenance; it was selected taking into account the resolution of the BX50 microscope. The hybrid RS 440-436 1.8º/step motor was employed, which permitted a minimum movement of two steps (3.6º), resulting in a 500 nm resolution. A RS 718-896 reduction box (100 to 1) was attached to the motor to enhance resolution to 5 nm, enough for optical-sectioning studies.

The reduction box was coupled to the motor by an adaptation kit provided by the manufacturer. Moreover, part of the fine adjustment knob was replaced by a similar piece that permits the attachment of the electro-mechanic system (by the external face of the reduction box) to the BX50 microscope. For simplicity and versatility, the system is controlled by parallel port by a personal computer, which enables easy data reading and writing, and has the additional advantage that it can be connected to any computer. Four parallel-port output lines were used to excite the stepping motor's coils (one for each coil) by excitation pulses generated by a computer program. In order to ensure the complete isolation of the computer and power circuits, optocouplers were used between the parallel-port output lines and the rest of the circuits. For a more detailed description of the design, please refer to [11]. The system is completely controlled by a program specially designed by our research group, called SUMMD (software for DDM users, from the Spanish "Software para Usuarios de Microscopia de Desconvolución Digital"). This software automatically performs optical-sectioning and image processing techniques (deconvolution and 3D reconstruction), once basic parameters are established [12]. Figure 2 is a photograph of the microscopy setup implemented in our laboratory

2.3 PSF determination

Optical-sectioning produces 3D image stacks containing in-focus and out-of-focus contributions. In order to keep only in-focus information, out-of-focus fluorescence must be either eliminated or restored to its correct spatial position, processes which require the optical system's transfer function, also known as Point Spread Function PSF. This function precisely describes the distortions a point source of light suffers when it is imaged by the optical system of the microscopy setup. It can be determined either theoretically (applying optic-geometry laws) or empirically (procedure detailed below). In order to perform empirical calculations, a point source of light must be simulated. Such source must not be too small so that it can not be resolved by the microscope or too big so that it no longer represents a point source. Since our work is based on fluorescence, fluorescent beads from the F-8888 kit (Molecular Probes, Eugene, OR, USA) were used as point sources of light; these beads have been specially designed for microscope alignment and calibration, and are therefore highly resistant to photobleaching [13]. The beads were coated by fluorophores with excitation/absortion peaks at 505/515 nm (same excitation peaks as for FITC, the yellow/green fluorophore used in our experiments). The original bead solution was diluted (1:100) so as to obtain disperse beads (and, therefore, images where a single one can be isolated and used as point source of light). The diluted solution was placed on a cover slip and after dry were covered by a coverslip which was later sealed with acrylic nail-polish for better stability.

In order for the bead to work as a point source of light (Dirac delta), its diameter must be approximately half the size of the first dark ring of the diffraction pattern (Airy disc) of the lens (lens resolution). Eq. (1) presents this condition

$$Bead\ diameter \leq 0{,}61\lambda / NA \quad (1)$$

where *NA* is the lens numerical aperture and λ is the wavelength of the emission peak. Once the bead size was determined, the PSF was obtained by optically-sectioning the selected bead at regular Z-intervals (displacement in the Z axis, which was selected so as to maintain a symmetric voxel), imaging as many planes above and below the focal plane as possible. In this way, distortions produced by the optical system can be captured and the Airy disc pattern can be quantified in a plane-by-plane basis. In order to obtain a good signal-to-noise ratio (SNR), the optical-sectioning procedure is repeated between three and five times in each focal plane; the averaged images are then normalized to produce the final stack corresponding to the PSF. Figure 3 shows the PSF for the 40X lens of the BX50 microscope. It is of utter importance to obtain the PSF under the same acquisition conditions the specimen under study is in.

2.4 Deconvolution

All imaging systems produce blurring independently of other forms of degradations (noise, dispersion and shine), either caused by the specimen or the system's electronics. This form of independence is the key to why blurring can be removed by deconvolution. Since blurring is a function of the microscope (mainly of the objective lens), it can be modeled with relative simplicity by algorithms derived from the mathematical analyses of the image formation process. This process is represented by the 3D convolution (symbolized by ⊗) of a known variable, the 3D PSF or PSF (x, y, z), and an unknown variable, the 3D distribution of fluorescence in the specimen *o*(x, y, z) [14-16]. The simplest form of the mentioned phenomenon is mathematically described in Eq. (2).

$$i\,(x, y, z) = \mathrm{PSF}\,(x, y, z) \otimes o\,(x, y, z) \quad (2)$$

where *i* (x, y, z) is the 3D image obtained by optical-sectioning. Several deconvolution algorithms (Table 1) may be used to try to reverse this process; they differ from one another by the way they work with out-of-focus data. Elimination algorithms subtract out-of-focus information, while restorations methods tend to reassign these contributions to their correct spatial position [17-19]. SUMMD software [12] includes the following deconvolution methods: *Nearest Neighbor*, *Regularized Linear Least Square, Inverse Wiener Filter* and *Constrained Iterative Deconvolution.*

Table 1. Deconvolution methods.

Name	Type	Category
- Nearest Neighbor	2D/Linear	Elimination
- Multiples Neighbors	2D/Linear	Elimination
- Wiener Filter	2D/Linear	Restoration
- Regularized Linear Least Square	3D/Linear	Restoration
- Non-Linear Least Square	3D/Non Linear	Restoration
- Constrained Iterative Deconvolution	3D/Iterative	Restoration
- Maximum Likelihood	3D/Iterative/Statistical	Restoration
- Constrained Maximum Likelihood	3D/Iterative/Statistical	Restoration
- Blind Deconvolution	3D/Iterative	Restoration

Nearest Neighbor is fundamentally 2D and eliminates information. It operates in a plane-by-plane basis, working individually on the 2D planes of a 3D stack. Briefly, it subtracts the out-of-focus contributions of the nearest planes to a given plane *o*, that is to say, *o±1*; this procedure is then repeated throughout the stack for all 2D planes. In this manner, an estimation of the out-of-focus information is eliminated from each plane. Elimination algorithms such as this are computationally simple and fast, yet they increase noise and reduce the level of fluorescent signal. Instead, *Regularized Linear Least Square* and *Inverse Wiener Filter* are restoration methods which work with the whole 3D stack. These are inverse algorithms which work in Fourier Space (instead of Image Space). Since a convolution in Image

Space is a mere multiplication in Fourier Space, these algorithms estimate the true distribution of fluorescence by dividing the Fourier Transform of an image stack by the Fourier Transform of the PSF. The usefulness of these methods is limited by noise amplification, since small variations in noise in Fourier Space are amplified during the mentioned division. Constrained iterative algorithms seek to improve the approach undertaken by inverse methods; such algorithms work in iterative cycles and apply restrictions to possible solutions. A typical constrained iterative algorithm works as follow. An estimate of the object is made (this is usually the raw image itself). The estimate is convolved with the PSF, and the resulting "blurred estimate" is compared with the raw image. This comparison is used to compute an error criterion that represents how similar the blurred estimate is to the raw image. This error criterion is then used to alter the estimate in such a way that the error is reduced. A new iteration then takes place; the new estimate is convolved with the PSF, a new error criterion is computed, etc. The best estimate will be the one that minimizes the error criterion; therefore, as long as the error criterion has not been minimized, each new estimate is blurred again; an error criterion is computed, etc. This process is repeated until the error criterion is minimized or reaches a defined threshold. The final restored image is the object estimate at the last iteration.

The performance and efficiency of the algorithms implemented by our research group have been presented in various congresses [20-22]. Results, which concur with those observed in other publications [23-24], demonstrate that elimination methods remove information. Since specimen images are highly random, it is difficult to estimate the proportion in which intensities are eliminated; this makes such algorithms inadequate for quantification procedures. Therefore, in the studies exposed in the present work, the *Positivity Constrained Iterative Deconvolution* restoration algorithm is used.

2.5 3D visualization and quantification

Stacks can be visualized using Maximum Intensity Projection (a graphic mode available in the SUMDD software) once images have been deconvolved and out-of-focus fluorescence has been restored to its correct spatial position. Additionally, quantification studies were performed. In order to identify the studied object (cell contacts indicated by the cell adhesion molecule E-cadherine), a model-based algorithm was used [25]. This method implemented a geometric model, with parameters which included minimum and maximum radius, minimum and maximum integrated intensity and signal's dynamic range. The lower limit of the dynamic range was selected so as to exclude background fluorescence (value obtained by plane-by-plane inspection), while the upper limit was the maximum intensity captured for CCD. The algorithm was implemented in MatLab 7 (MathWorks, Inc.). Briefly, the whole stack is analyzed in search for a voxel with intensity within the dynamic range; if such voxel is found, then the integrated intensity is evaluated. If all criteria are met, then the voxel is recognized as a useful point, it is compute and its spatial position is logged.

Fig. 2: DDM system designed and developed in the Microscopy Laboratory (FI-UNER), used to perform 3D studies.
1 – Olympus BX-50 epifluorescence microscope.
2 – CDD camera.
3 – Electro-mechanic control.
4 – Electronic module.
5 – Control computer.
6 – Computer used to process and analyze images.

3. Evaluation

Once the development of the electro-mechanic system (responsible for the displacement in the Z axis involved in optical-sectioning) and the SUMDD software (which controls all procedures) were concluded, and after the PSF determination was validate, the technique's usefulness was evaluated.

3.1 PSF determination and geometry

In order to obtain a good 3D image with the conventional systems mentioned (which have not been designed *a priori* with this goal), the optical path must not be significantly altered. Therefore, specimens must by observe in systems where the refractive index of the mounting medium, coverslip and immersion medium are identical for all wavelengths of interest. In practice, the aforementioned conditions are not always met, and unfortunately, thick specimens worsen the situation. Thus, optimal conditions must be determined for each specimen. We have demonstrated recently [26] that an easy and practical way to achieve such conditions is accomplished by varying parameters until obtaining the most symmetrical PSF possible (symmetrical in all three axis).

In the present work, we corroborated that the PSF is made up of a set of concentric rings in XY projections (Fig. 3A) and that it exhibits an hour-glass profile in XZ and YZ projections (Fig. 3B); these results concur with others observed for different types of optical systems [27]. The PSF was determined under the ideal conditions for which the objective lens was designed. For all lens, we used a glass coverslip (refractive index: 1.51; thickness: 170 μm) and a mounting medium specifically developed with this goal (VectaShield, Vector Labs.). Additionally, in the case of the 100X immersion-oil lens, immersion oil produced by the manufacturer of the lens was used (refractive index: 1.518); results obtained with this lens (not shown) are similar to those presented in Figure 3.

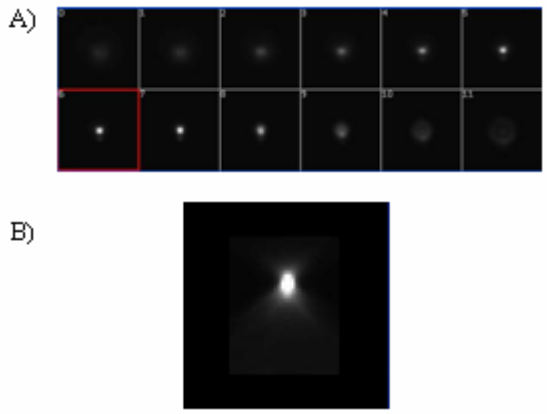

Fig. 3: Shape and geometry of a PSF experimentally determined for the 40X 0.85 NA lens of the BX50 microscope.
A) XY projections (32x32 pixels^2) of a sphere of 0,46 μm of diameter. Each section is separated by a ΔZ of 0.5 μm. The red frame denotes the focus plane; the concentric rings of the Airy pattern become more noticeable as we move away from the focus plane.
B) XZ projection, using the Maximum Intensity Projection method. The hour-glass shape is clearly noticed.

We can conclude that empirical PSFs of the BX50 microscope (40X and 100X lens) do not present perfect symmetry (Fig. 3). As a general rule, the better the alignment and lens quality, the more symmetrical the PSF (it resembles its ideal shape more). Since objectives lens used are plan-apochromatic and corrected for chromatic, spherical and curvature aberrations, and since the alignment is a routine practice that does not represent greater conflicts, we deduce that the PSF asymmetry must be a consequence of problems in the optical path. This was verified by evaluating the PSF under different 3D optical arrangements. Figure 4A and 4B show various PSFs obtained by varying coverslip thickness and correction collar values (40X lens), respectively. Results obtained when altering other parameters are analyzed in [26].

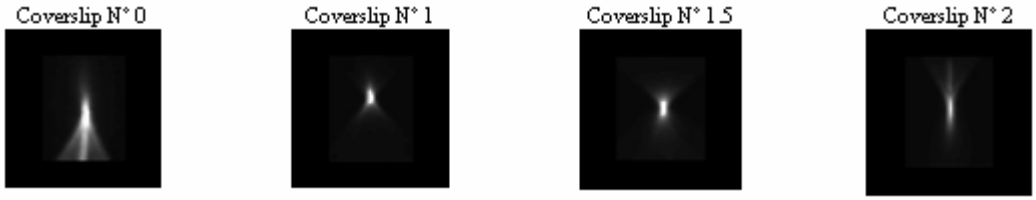

Fig. 4A: XZ projection of the PSF determined with a 40X 0.85 NA lens, using different coverslips thickness. In each case, conic figures with various degrees of asymmetry respect to the focal plane are observed.

Fig. 4B: XZ projection of the PSF determined with a 40X 0.85 NA lens, using different correction collar values. In each case, conic figures with various degrees of asymmetry respect to the focal plane are observed.

The most symmetrical PSF was obtained when using the lens in the conditions for which they were designed in all evaluated cases.

3.2 Restoration by deconvolution

The 3D image of a sphere will present elongation in the Z axis due to optical-sectioning and diffraction problems; deconvolution aims to reduce this elongation and restore the sphere's original dimensions. In order to quantify elongation and elongation reduction post-deconvolution, a patron specimen of known shape and size was used (fluorescent beads similar to the ones used to obtain the PSF, of 4 μm of diameter). A unique deconvolution method was used for all conditions and elongation was measured using the FWHM (Full Width at Half Maximum) technique [28].

Figure 5 and 6 show PSF elongation and elongation reduction post deconvlution (100X lens) for PSFs determined using different coverslip thickness and immersion mediums, respectively. In both figures, bar 1 represent the elongation before deconvolution; this value was used in the statistical analysis. An extremely significant elongation reduction was observed for all coverslips after deconvolution; even though there are no significant differences between coverslips, N°1.5 y N°2 present the greatest reductions (30% and 32%, respectively). In addition, extremely significant elongation reduction was observed for all immersion mediums; even though there are no significant differences between mediums, immersion oil (refractive index 1.51) presented the greatest reductions (32%).

Based upon the results obtained, we can conclude that the deconvolution algorithm is working properly, since the out-of-focus fluorescence that caused the elongation (over 3 μm) was reassigned to its correct spatial position, reducing the diameter of the sphere (elongation below 1 μm)

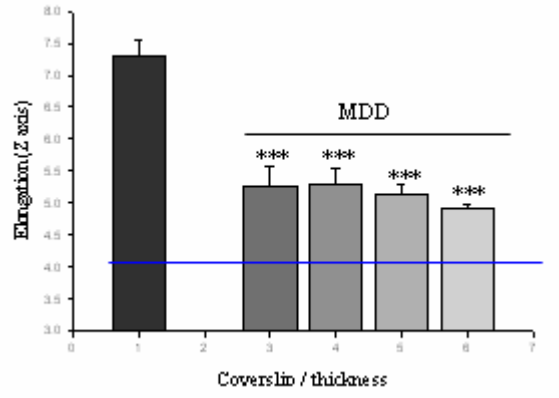

Fig. 5: 3D quantification of the elongation in the Z axis. Bar 3: PSF determined with coverslip N°0: (80 – 120 μm of thickness). Bar 4: PSF determined with coverslip N°1: (130 – 160 μm of thickness). Bar 5: PSF determined with coverslip N°1.5: (160 – 190 μm of thickness). Bar 6: PSF determined with coverslip N°2: (190 – 220 μm of thickness). The blue line represents the real diameter of the bead. Values shown represent the medium ± standard deviation, n = 4. The data was analyzed by an ANOVA *a posteriori* Tukey-Kramer test: *** $p<0.001$.

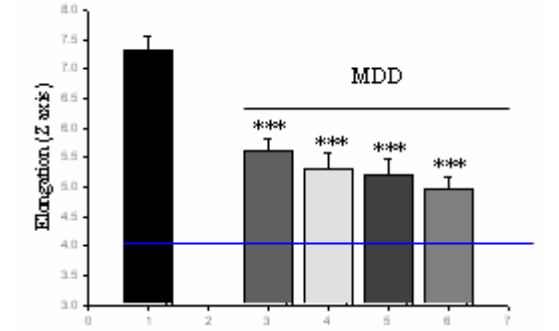

Fig. 6: 3D quantification of the elongation in the Z axis. Bar 3: PSF determined using air as immersion medium (η=1). Bar 4: PSF determined using water as immersion medium (η=1.33). Bar 5: PSF determined using glycerin as immersion medium (η=1.47). Bar 6: PSF determined using immersion oil as immersion medium (η=1.51). The blue line represents the real diameter of the bead. Values shown represent the medium ± standard deviation, n = 4. The data was analyzed by an ANOVA *a posteriori* Tukey-Kramer test: *** $p<0.001$.

4. Application using a biological model

As an example of experimental validation of the system, the mentioned technique was applied using a biological model commonly used in the Microscopy Laboratory of the FI-UNER. The expression pattern of the cell-adhesion molecule E-cadherinwas studied in skin of stage 19 *Bufo arenarum* tadpole embryos. Previous studies by our research group [29] have identified a lineal and uniform distribution pattern of E-cadherinin the cell perimeter. The importance and relevance of these investigations relay on the fact that many cellular functions depend on the spatial and temporal regulation of cell-adhesion molecules [30-33]. Until now, all related studies have been done in 2D; nevertheless, the spatial-location regulation must be studied in order to elucidate the role of E-cadherine. The application of the technique presented in the present work enabled us to undertake the 3D aspect of this model for the first time.

When sectioning a whole stage 19 embryo (approximately 1500 μm of thickness), out-of-focus information made it difficult to distinguish the genuine fluorescent marks and distribution pattern of E-cadherin(Fig. 7A). After deconvolution was applied (Fig. 7B), out-of-focus fluorescence reassignment unveiled a punctual pattern, where each bright dot represented a cell-cell contact. Using the abovementioned quantification algorithm, information regarding focal contacts was saved; this enabled a geometrical and spatial distribution analysis. Figure 8 shows two 3D perspectives of the spatial distribution of E-cadherinin epidermal epithelium. Cluster disposition concurs with recent results obtained with other techniques [34-37].

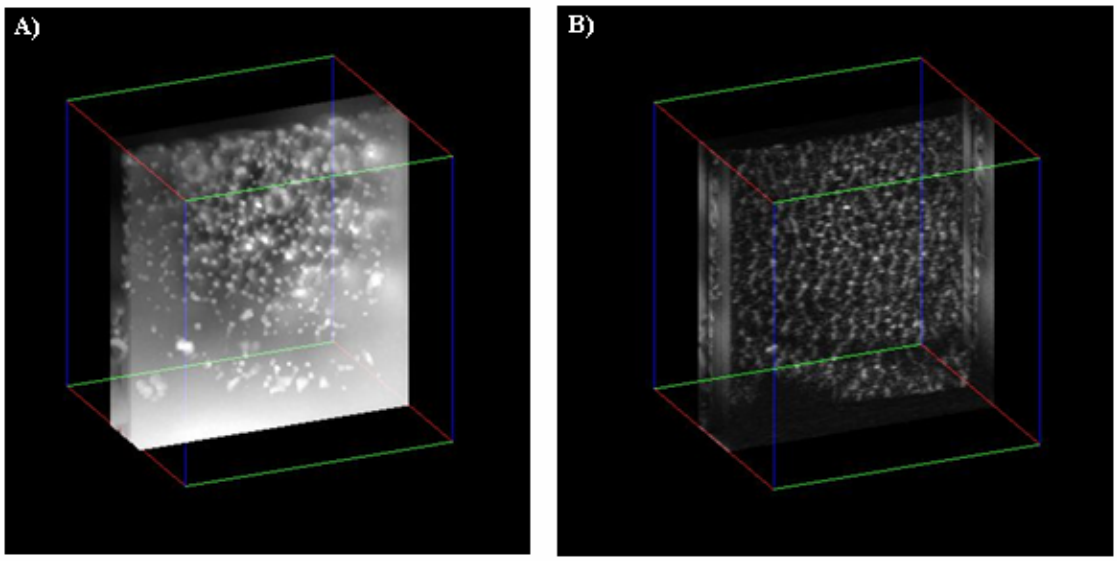

Fig. 7: Tilted view of a 3D representation of the epidermis of a *Bufo arenarum* embryo. The distribution pattern of E-cadherinis observed before (A) and after (B) deconvolution. Green lines (X axis), blue lines (Y axis), red lines (Z axis).

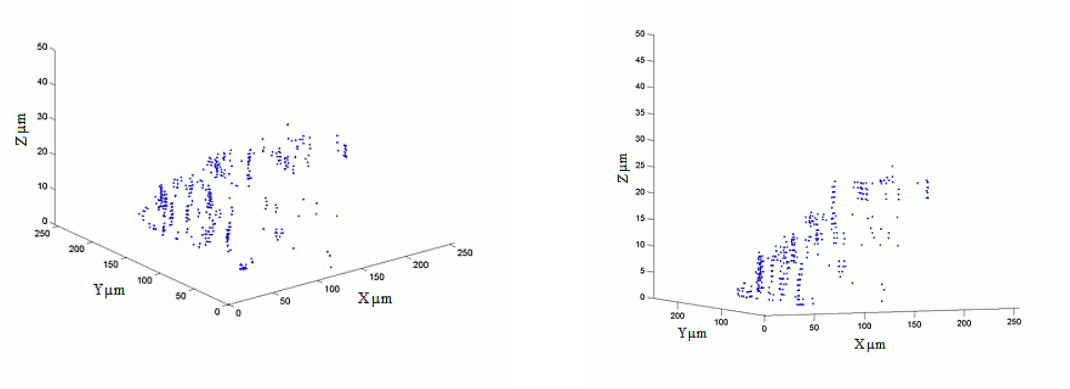

Fig. 8: Two 3D perspective views of cell-cell contacts marked by E-cadherin in epidermal epithelium of a stage 19 *Bufo arenarum* embryo. Presented points are the result provided by the quantification algorithm which was specially designed to identify the clusters of E-cadherin.

5. Impact

The technique described and implemented in the present work by our research group demonstrates to be an excellent and economic alternative to perform 3D studies. The mechanical adaptations proposed can be implemented in any type of microscope (with minor modifications), which justifies the development exposed.

Digital deconvolution microscopy presents some clear advantages. DDM has higher detection efficiency than confocal laser microscopy, since it uses a CCD camera instead of a photomultiplier tube. Additionally, in spite of having similar high-frequency attenuation in raw images, DDM may achieve greater effective resolution (compared to raw confocal images) since deconvolution corrects this

attenuation. On the other hand, a disadvantage is that DDM requires specially trained personnel since it strongly depends on the correct PSF determination and deconvolution algorithms employed.

The implementation of this technology has enabled us to undertake 3D studies, which in turn leads our research group to revise and discuss new visualization and quantification methologies. The different 3D visualization modes (surface rendering, animation and maximum intensity projection) can be employed to view the spatial distribution of various structures. The quantification process implies new challenges; this is why several models that are congruent with the biological functions of cell-adhesion molecules and at the same time improve the representation of the distribution of these in skin, are currently being explored and enhanced. Innovative experiments are being carried out with this goal in mind; new PSF determination strategies are being evaluated and deconvolution algorithm are being optimized. With these, we intend to apply the deconvolution process to images obtained from a confocal laser microscope, which would improve axial resolution even more.

Acknowledgements: the present work was developed with funds from research projects 6067-1 and 6082-1 of the National University of Entre Ríos (UNER), and has been entirely developed by personnel and with infrastructure of the Microscopy Laboratory of the FI-UNER.

References

[1] J. Adur, F. Balducci, J.C. García, J. Vilá, M.F. Izaguirre and V. Casco, Ciencia Hoy **11**, 22 (2001)
[2] C. Vonesch, F. Aguet, J. Vonesch and M. Unser, IEEE Signal Processing Magazine **5**, 21 (2006)
[3] F. Difato, F. Mazzone, S. Scaglione, M. Fato, F. Beltrame, L. Kubinova, J. Janacek , P, Ramoino, G. Vicidomini, A. Diaspro, Microsc Res Tech **64**, 151 (2004)
[4] B. Sprague, F. Muller, R. Pego, P. Bungay, D. Stavreva, J. McNally, Biophys J **91,** 1169 (2006)
[5] J. Conchello and J. Lichtman, Nature Methods **2**, 920 (2005)
[6] D. Biggs, Biophotonics **2**, 1 (2004)
[7] M. Laurent, G. Johannin, N. Gilbert, L. Lucas, D. Cassio, P. Petit, A. Fleury, Biol Cell **80**, 29 (1994)
[8] D. Fung, J. Theriot, Current Opinion in microbiology **1**, 346 (1998)
[9] P. Andrews, I. Harper, J. Swedlow, Traffic **3**, 29 (2002)
[10] Y. Hiraoka, J. Sedat, D. Agard, Science **238**, 36 (1987)
[11] J. Adur, Tesis de Graduacion (1997)
[12] J. Diaz Zamboni, Tesis de Graduación (2004)
[13] Y. Zhang, D. Carter, Applied Immunohistochemistry & Molecular Morphology **7**, 156 (1999)
[14] K. Castleman, Digital Image Processing. Prentice-Hall, Inc. Eds. (1996)
[15] P. Jansson, Deconvolution of Images and Spectra, Second Edition, Academic Press (1997)
[16] J. McNally, T. Karpova, J. Cooper, J. Conchello, Methods **19**, 373 (1999)
[17] C. Preza, M. Miller, L. Thomas, J. McNally, Journal of the Optical Society of America. A. **9**, 219 (1992)
[18] Y. Wang, Methods in Cell Biology **56**, 305 (1998)
[19] W. Wallace, L. Schaefer, J. Swedlow, Biotechniques **31**, 1076 (2001)
[20] A. Cherniz, J. Adur, G. Deluca, V. Casco, Proceedings of SADIO Santa Fe, Argentina (2002)
[21] J. Díaz-Zamboni, J. Adur, F. Balducci, A. Cherniz, M.F. Izaguirre, V. Casco, Proceedings of XIV Congreso Argentino de Bioingeniería. SABI 2003. Argentina. (2003).
[22] J. Díaz-Zamboni, J. Adur, V. Casco, Proceedings of Sociedad Venezolana de Métodos Numéricos en Ingeniería, Simulación Numérica y Modelado Computacional. 17, (2004)
[23] J. Conchello, Cell Image Methods Express, Stevens Ed, 181 (2005)
[24] J. Sibarita, Advanced Biochemistry Engineering and Biotechnology **95**, 201(2005)
[25] T. Cootes, in Baldock R and Graham J Eds. Oxford University Press, Chap 7, 223-247 (2000)
[26] J. Adur, Tesis para obtener el titulo de Maestria, Inedita. UNER. Octubre (2006)
[27] B. Scalettar, J. Swedlow, J. Sedat, D. Agard, Journal of Microscopy **182**, 50 (1996)
[28] M. Kozubek, Microscopy Research and Technique **53**, 157 (2001)
[29] M.F. Izaguirre, Tesis para obtener el titulo de Doctor en Biología. Inedita. U.N.L. Diciembre (2003)
[30] T. Jessell, Neuron **1**, 3 (1988)
[31] M. Hortsch, C. Goodman, Annual review of cell biology **7**, 505 (1991)
[32] E. Vitetta, M. Berton, C. Burger, M. Kepron, W. Lee, X. Yin, Annual Review of Immunology **9**, 193 (1991)

[33] M. Kosco, D. Gray, Immunological reviews **126**, 63 (1992)
[34] C. Schreider, G. Peignon, S. Thenet, J. Chambaz, M. Pincon-Raymond, Journal of cell science **115**, 543 (2002)
[35] S. Murase, S. Hirano, X. Wang, M. Kitagawa, M. Natori, S. Taketani, T. Suzuki, Biochemical and Biophysical Research Communications **276**, 1191 (2000)
[36] A. Kusumi, K. Suzuki, K. Koyasako, Current Opinion in Cell Biology **11**, 582 (1999)
[37] S. Sivasankar, W. Brieher, N. Lavrik, B. Gumbiner, D. Leckband, Proceedings of the National Academy of Sciences of the United States of America **96**, 11820 (1999)